

RESEARCH ARTICLE | NOVEMBER 06 2025

Evaluation of stress tensor around a threading defect in diamond: Application of NV center-based measurement and comparative multi-modal analysis ^{EP}

Takeyuki Tsuji  ; Shunta Harada  ; Tokuyuki Teraji  *J. Appl. Phys.* 138, 174401 (2025)<https://doi.org/10.1063/5.0292833>

Articles You May Be Interested In

Nondestructive analysis of threading mixed dislocations in SiC using x-ray topography and birefringence

AIP Advances (February 2025)

Focused light birefringence for three-dimensional observation of dislocations in silicon carbide wafers

Rev. Sci. Instrum. (August 2025)

Nanotechnology & Materials Science



Optics & Photonics



Impedance Analysis



Scanning Probe Microscopy



Sensors



Failure Analysis & Semiconductors



Unlock the Full Spectrum. From DC to 8.5 GHz.

Your Application. Measured.

[Find out more](#)

Evaluation of stress tensor around a threading defect in diamond: Application of NV center-based measurement and comparative multi-modal analysis

Cite as: J. Appl. Phys. **138**, 174401 (2025); doi: [10.1063/5.0292833](https://doi.org/10.1063/5.0292833)

Submitted: 24 July 2025 · Accepted: 15 October 2025 ·

Published Online: 6 November 2025



Takeyuki Tsuji,¹  Shunta Harada,^{2,3}  and Tokuyuki Teraji^{4,a)} 

AFFILIATIONS

¹International Center for Young Researchers, National Institute for Materials Science, 1-1 Namiki, Tsukuba, Ibaraki 305-0044, Japan

²Center for Integrated Research of Future Electronics (CIRFE), Institute of Materials and Systems for Sustainability (IMaSS), Nagoya University, Furo-cho, Chikusa-ku, Nagoya 464-8601, Japan

³Department of Materials Process Engineering, Nagoya University, Furo-cho, Chikusa-ku, Nagoya 464-8603, Japan

⁴Research Center for Electronic and Optical Materials, National Institute for Materials Science, 1-1 Namiki, Tsukuba, Ibaraki 305-0044, Japan

^{a)}Author to whom correspondence should be addressed: TERAJI.Tokuyuki@nims.go.jp

ABSTRACT

Threading defects in diamond degrade the performance of diamond-based quantum and electronic devices. Although the disorder of the atomic arrangement induced by the threading defects is considered to be the cause of the performance degradation, yet quantitative and spatially resolved evaluation of the stress tensor that characterizes the magnitude of the disorder has remained challenging. In this study, we applied the evaluation technique of the stress tensor based on nitrogen-vacancy (NV) centers to the mapping of the stress field around a threading defect in a chemical vapor deposition diamond film. Furthermore, we compared the stress tensor measured using NV centers with that obtained by conventional methods such as Raman spectroscopy and x-ray topography. Around the threading defect, the components of the stress tensor σ_{xy} , σ_{yz} , σ_{zx} , and $\sigma_{xx} + \sigma_{yy} + \sigma_{zz}$ varied by approximately 0.2, 0.2, 0.3, and 1.2 GPa, respectively, and each component exhibited a rotationally symmetric distribution extending over a diameter of approximately 10–20 μm . We calculated the Raman shift mapping from the stress tensor obtained using NV centers, and the Raman peak was estimated to decrease by approximately 0.9 cm^{-1} due to the stress tensor at the center of the threading defect. This value was comparable to the experimental result of Raman shift mapping. These results indicate that the components of the stress tensor measured by NV centers accurately reflect the stress induced by the threading defects. The stress tensor and x-ray topography images suggest that the threading defect measured in this study was a bundle dislocation.

© 2025 Author(s). All article content, except where otherwise noted, is licensed under a Creative Commons Attribution (CC BY) license (<https://creativecommons.org/licenses/by/4.0/>). <https://doi.org/10.1063/5.0292833>

INTRODUCTION

Diamonds are known as one of the promising materials for electronic^{1,2} applications because diamond has excellent electronic properties with wide bandgap, high carrier mobility, and high thermal conductivity.³ Nitrogen-vacancy (NV) centers in diamonds are color centers with unique quantum properties^{4–6} and expected to be applied to quantum sensors,^{7,8} networks,^{9–11} and computers.^{6,12} Regarding quantum sensor applications, NV centers are

sensitive to several external fields, such as magnetic fields,^{13,14} electric fields,^{15,16} and temperature.^{17,18}

Homoeptitaxial chemical vapor deposition (CVD) diamond films typically contain threading defects propagated from the substrate such as dislocations in the range of 10^2 – $10^6/\text{cm}^2$, while heteroepitaxial diamond films contain those of over $10^6/\text{cm}^2$.^{19–21} Threading defects such as dislocations degrade the performance of electronic and quantum applications. In electronic applications, it

27 November 2025 07:04:33

is well known that local disruptions in the atomic structure at the core of these defects induce midgap states within the bandgap, causing leakage currents.^{19,22–24} In addition to the deterioration of crystal quality in the threading defects themselves, we consider that the stress fields around these threading defects can alter the semiconductor properties of diamond and even promote the formation of additional threading defects. Through evaluating the stress field around threading defects, we expect to clarify the influence of the stress field on semiconductor properties and the formation of threading defects. In the case of quantum application, the stress alters the energy levels of the NV centers,^{25,26} which deteriorates the properties of the quantum network²⁷ and computers.²⁸ In addition, inhomogeneous energy levels of NV centers lead to a decrease in the spin dephasing time T_2^* of the NV centers,²⁹ which deteriorates the sensitivity of quantum sensors.⁴ Therefore, it is technologically essential to reduce threading defects in the CVD diamonds. For this purpose, the evaluation of the stress caused by the threading defect is important.

Stress in a crystal is applied along the x axis, y axis, and z axis, corresponding to the x -plane, y -plane, and z -plane, respectively, in the three-dimensional space as shown in Fig. 1(a). Thus, the stress in a crystal is primarily presented as the following matrix, known as the stress tensor:

$$\begin{bmatrix} \sigma_{xx} & \sigma_{xy} & \sigma_{xz} \\ \sigma_{xy} & \sigma_{yy} & \sigma_{yz} \\ \sigma_{xz} & \sigma_{yz} & \sigma_{zz} \end{bmatrix}. \quad (1)$$

This tensor contains six independent components including axial stress (σ_{xx} , σ_{yy} , σ_{zz}) and shear stress (σ_{xy} , σ_{yz} , σ_{zx}) [Figs. 1(b) and 1(c)]. Thus, measuring the stress tensor is important to evaluate the stress field in the diamond. Despite its importance, measuring the components of the stress tensor has been a challenging task for conventional methods including Raman spectroscopy,³⁰ birefringence microscopy,³¹ and x-ray diffraction.³² In each of these techniques, the measurement output data related to stress are only one—such as the peak shift of Raman emission, phase difference, or change in the diffraction angle—making it difficult to uniquely determine the components of the stress tensor. Thus, in the case of Raman spectroscopy, stress in the crystal has been evaluated assuming a hydrostatic pressure ($\sigma_{xx} = \sigma_{yy} = \sigma_{zz}$, $\sigma_{xy} = \sigma_{yz} = \sigma_{zx} = 0$).

In contrast, in this study, the components of the stress tensor were directly extracted by employing NV centers in diamond. This method has already been demonstrated in previous studies.^{33–35} NV centers are a color center with a spin-1 electronic ground state, consisting of one nitrogen and one vacancy in diamond. The two resonance frequencies of a single NV center, i.e., differences in the energy levels between $m_s = 0$ and $m_s = +1$ and between $m_s = 0$ and $m_s = -1$, can be read out by microwave irradiation and detecting the fluorescence intensity. This scheme is called optically detected magnetic resonance (ODMR).³⁶ These two resonance frequencies are varied depending on the stress tensor applied to the NV center. As shown in Fig. 1(d), the NV center arranges in four directions ($i = 1, 2, 3, 4$) depending on the positional relationship between the nitrogen and the vacancy. Thus, we can reconstruct the components (σ_{xy} , σ_{yz} , σ_{zx} , $\sigma_{xx} + \sigma_{yy} + \sigma_{zz}$) of the stress tensor by reading out a total of 2×4 (directions) = 8 resonance frequencies varied by the stress tensor. In a previous study, components of the stress tensor

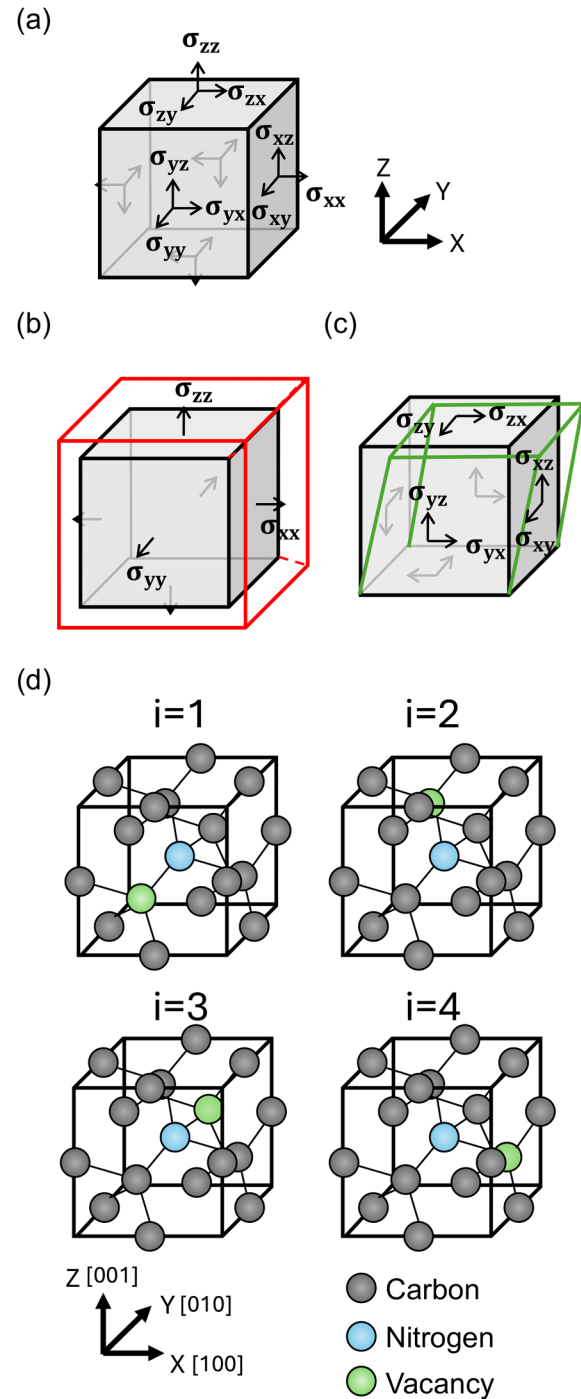


FIG. 1. (a) Schematic of the unit cell of the crystal and stress. (b) Schematic of the unit cell of the crystal under axial stress components (σ_{xx} , σ_{yy} , σ_{zz}): A crystal subjected to axial stress, transitioning from a black to a red cell. (c) Schematic of the unit cell of the crystal under shear stress components (σ_{xy} , σ_{yz} , σ_{zx}): A crystal subjected to shear stress undergoes, transitioning from a black to a green cell. (d) NV centers in the diamond arranged in the four different axes.

27 November 2025 07:04:33

induced by scratches, implantation damage, nanoindents, and devices fabricated on diamond were measured using this technique.^{34,35}

In this study, we applied the stress tensor measurement technique based on NV centers to measure the stress tensor around a threading defect in the CVD diamond film. The stress tensor obtained using NV centers was compared with that obtained by a conventional method, Raman spectroscopy, to verify the validity of the NV-center-based measurements. Finally, the stress tensor obtained in this study, together with x-ray topography images, was used to clarify the structure of the threading defect.

METHODS

We characterized the threading defect in the nitrogen-doped homoepitaxial CVD diamond film with a thickness of 20 μm . A high-pressure and high-temperature (HPHT) type-Ib (001) single crystal with a thickness of 500 μm was used as a substrate. The top surface of the substrate was mechanically polished along the [110] direction under a fine polishing condition. The CVD growth condition was as follows: 110 Torr reaction pressure, 1.4 kW microwave power, 10% ^{12}C purified methane concentration ratio (flow rate ratio of CH_4 to the total gas flow), 0.2% nitrogen concentration ratio (flow rate ratio of N_2 to the total gas flow), 2% oxygen concentration (flow rate ratio of O_2 to the total gas flow), and 1020–1090 $^\circ\text{C}$ substrate temperature. The oxygen adding growth condition was applied because oxygen adding has a role in decreasing the number of newly generated dislocations in the CVD diamond films.^{37–39} Figure 2(a) shows the optical microscope image of the CVD diamond film. The step-bunching feature was observed along the [110] direction, indicating that nitrogen was doped in the CVD diamond film.⁴⁰ Figures 2(b) and 2(c) show the birefringence images taken at the same position before (HPHT substrate) and after CVD growth, respectively. In Figs. 2(b) and 2(c), petal-shaped birefringence patterns were observed at the same position, confirming the presence of a threading defect that propagated from the HPHT substrate into the CVD diamond film.

The fluorescence from NV centers around the threading defect was detected using a confocal microscope as shown in Fig. 2(d). We used a 514 nm laser with polarization aligned in the [010] direction. Figure 2(e) shows the fluorescence image in the cross section (XZ plane) of the CVD film using the confocal microscope. The high intensity region in Fig. 2(e) indicated the CVD diamond film with NV centers. Figure 2(f) shows the fluorescence images in the XY plane of the CVD diamond film at a depth of approximately 10 μm from the surface of the CVD diamond film. The threading defect observed by the birefringence image was located near the center of this image. The continuous-wave ODMR measurements were performed at the laser power of approximately 4 mW. The copper wire with a diameter of 20 μm was used for microwave irradiation. The wire was placed so as to be parallel to the [010] direction, and all ODMR measurements were performed at approximately 30 dBm. Figure 2(g) shows the ODMR spectra measured at positions P and Q in Fig. 2(f). Position P indicates the measurement location close to the threading defect, while point Q represents the location farther from the defect. The resonance frequencies were varied by approximately 1–3 MHz between locations P and Q. This change in frequencies was due to the change the

stress tensor between the positions P and Q. The eight resonance frequencies ($f_{\pm i}$) ($i = 1, 2, 3, 4$) were determined by fitting the ODMR spectrum with eight Lorentzian functions. Here, i denotes the number corresponding to the direction of the NV center, as shown in Fig. 1(d). We defined S_i as

$$S_i = \frac{f_{+i} + f_{-i}}{2}. \quad (2)$$

We determined the three shear stress components (σ_{xy} , σ_{yz} , σ_{zx}) and trace of the stress tensor ($\sigma_{xx} + \sigma_{yy} + \sigma_{zz}$) using the following equations:³⁴

$$\sigma_{xy} = \frac{S_1 - S_2 - S_3 + S_4}{8a_2}, \quad (3)$$

$$\sigma_{yz} = \frac{S_1 + S_2 - S_3 - S_4}{8a_2}, \quad (4)$$

$$\sigma_{zx} = \frac{S_1 - S_2 + S_3 - S_4}{8a_2}, \quad (5)$$

$$\sigma_{xx} + \sigma_{yy} + \sigma_{zz} = \frac{\frac{S_1 + S_2 + S_3 + S_4}{4} - D}{a_1}, \quad (6)$$

where the stress susceptibility parameters are $a_1 = 4.86$, $a_2 = -3.7$ (MHz/GPa). (The derivation of these equations was described in the [supplementary material](#)). The measurement error of the components of the stress tensor was calculated using the equation shown below:

$$S_{i\text{error}} (i = 1, 2, 3, 4) = \sqrt{(f_{+i\text{err}})^2 + (f_{-i\text{err}})^2} / 2, \quad (7)$$

$$\sigma_{xy\text{-error}} = \sigma_{yz\text{-error}} = \sigma_{zx\text{-error}} = \sqrt{\sum_{i=0}^4 (S_{i\text{error}})^2 / 8a_2}, \quad (8)$$

$$\sigma_{xx} + \sigma_{yy} + \sigma_{zz\text{-error}} = \sqrt{\sum_{i=0}^4 (S_{i\text{error}})^2 / 4} / a_1, \quad (9)$$

where $f_{+i\text{err}}$ and $f_{-i\text{err}}$ were the fitting error of the resonance frequencies ($f_{\pm i}$). Here, compressive stress and tensile stress were defined as positive and negative, respectively. Finally, by scanning the sample stage with respect to the laser irradiation position and measuring the resonance frequency at each sample position according to the procedure described above, the mapping of the stress tensor components around the threading defect was obtained. The acquisition time per pixel, as well as the pixel dwell time, was 3 min. We measured the stress tensor at 40×40 points over a region of 30 μm along the X = [100] axis and 25 μm along the Y = [010] axis around the threading defect. Thus, the total acquisition time was approximately 80 h.

27 November 2025 07:04:33

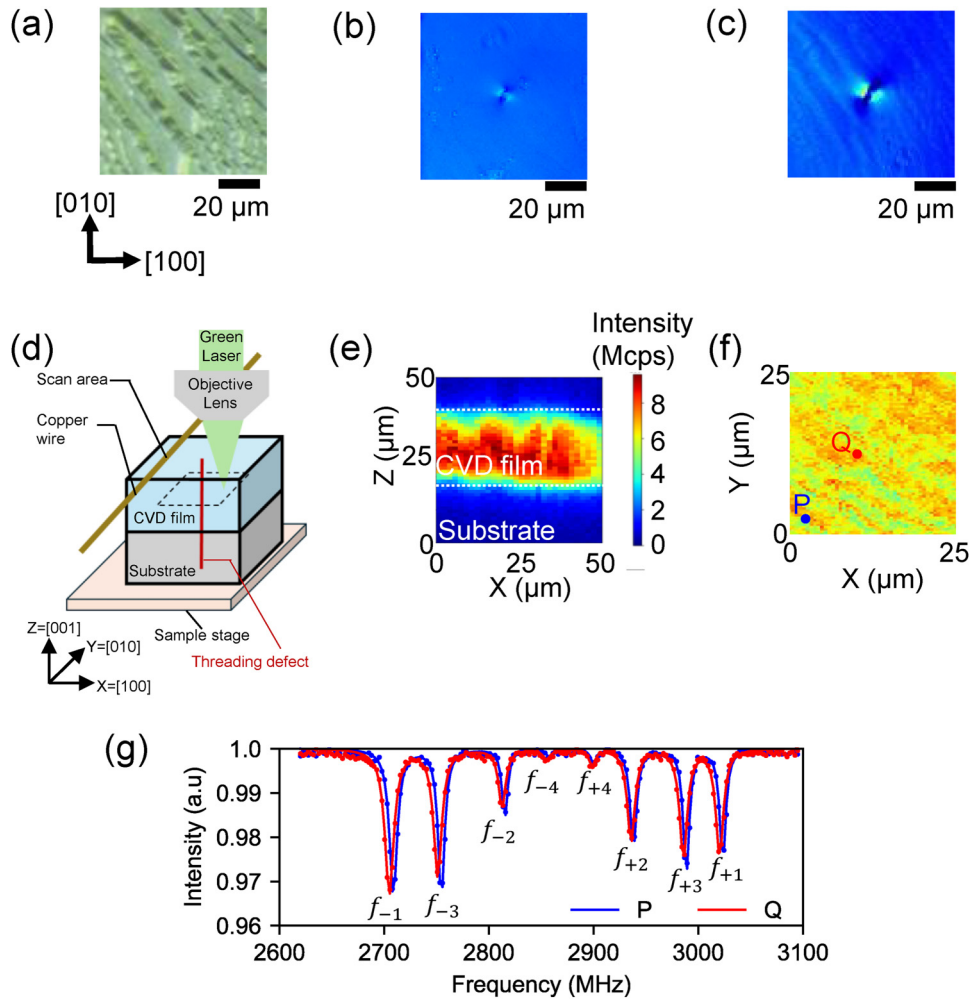


FIG. 2. (a) Optical microscope image of the CVD diamond film. (b) and (c) Birefringence images measured at the surface of the HPHT diamond substrate and CVD diamond film, respectively. (d) Schematic of a confocal microscope for measuring the stress tensor field around the threading defect. By moving the sample stage with the diamond, the fluorescence detection point was moved around the threading defect. (e) The fluorescence image in the cross section (XZ plane) of the CVD film using the confocal microscope. (f) The fluorescence image of the XY plane within the CVD diamond film ($z = 25 \mu\text{m}$). (g) ODMR spectra at measured at positions P and Q in (f).

27 November 2025 07:04:33

RESULTS AND DISCUSSION

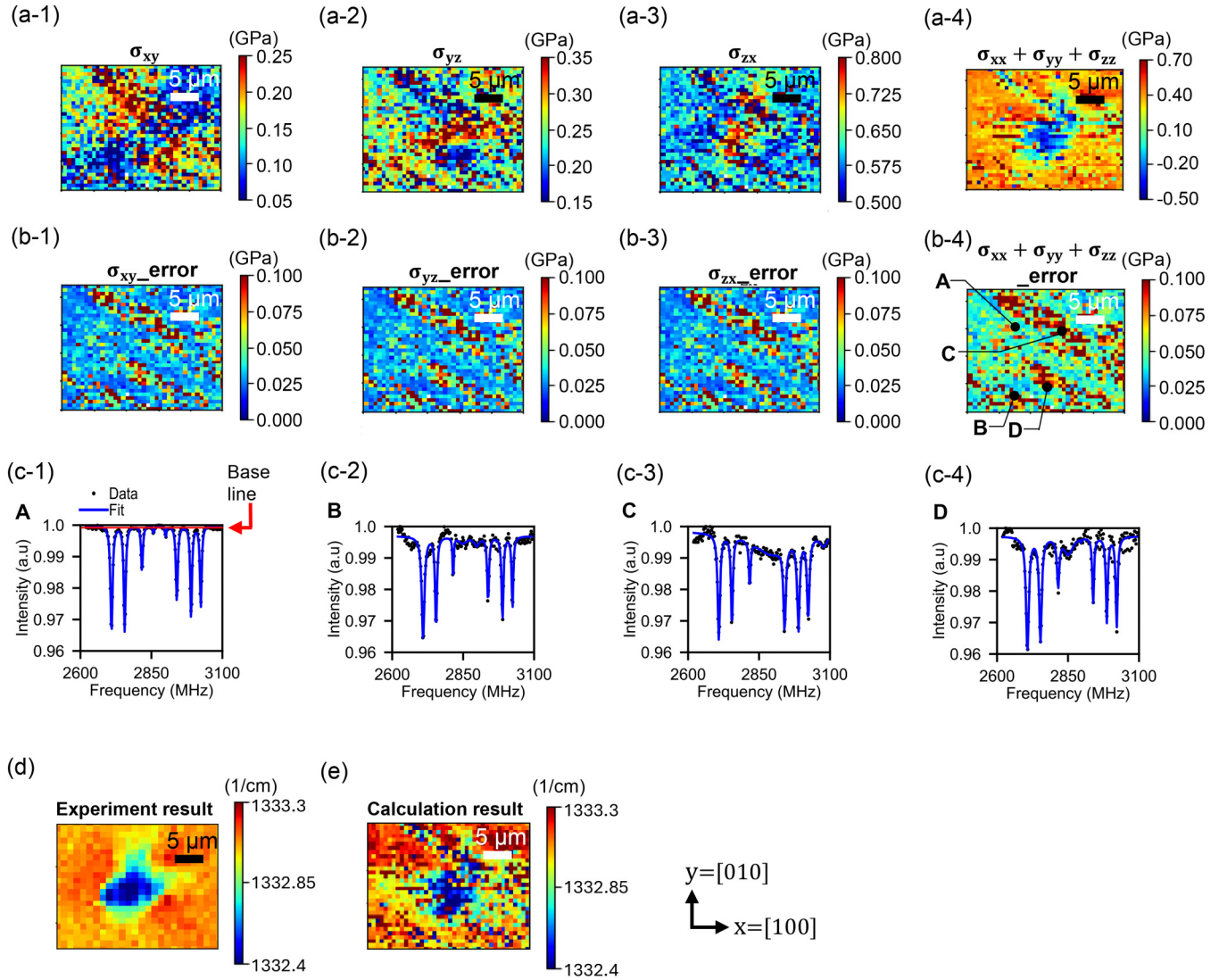
Mapping of stress tensor

Figures 3(a-1)–3(a-4) show the spatial map of components of the stress tensor, σ_{xy} , σ_{yz} , σ_{zx} and $\sigma_{xx} + \sigma_{yy} + \sigma_{zz}$, around the threading defect, respectively. The variation in the magnitude of the stress of the components, σ_{xy} , σ_{yz} , σ_{zx} and $\sigma_{xx} + \sigma_{yy} + \sigma_{zz}$, was approximately 0.2, 0.2, 0.3, and 1.2 GPa, respectively. Thus, we found that the trace of the stress tensor ($\sigma_{xx} + \sigma_{yy} + \sigma_{zz}$) was the dominant stress induced by the threading defect. The distribution of the components of shear stress, σ_{xy} , σ_{yz} , σ_{zx} , exhibited a point-symmetrical stress distribution with respect to the center of the threading defect. As described in the [supplementary material](#), the stress tensor of a single dislocation has a petal-like symmetrical distribution. In addition, the variation in signal contrast in the birefringence image is sensitive to the distribution of the in-plane shear stress component of σ_{xy} .⁴¹ The spatial variation in signal contrast observed in the birefringence image of the diamond CVD film shown in Fig. 2(c) was comparable to the distribution of σ_{xy}

measured using NV centers, as shown in Figs. 3(a-1). Thus, it is reasonable that such a symmetrical stress distribution was observed around the threading defect in this study. It should be noted that the birefringence image reflected the stress integrated from the substrate up to the surface of the CVD film, whereas the stress tensor shown in Figs. 3(a-1)–3(a-4) presented the in-plane stress at a depth of approximately $10 \mu\text{m}$ from the surface of the CVD diamond film.

Regarding the components of the trace of the stress tensor, $\sigma_{xx} + \sigma_{yy} + \sigma_{zz}$, shown in Fig. 3(a-4), we found that the tensile stress of approximately 1.2 GPa was applied at the center of the threading defect comparing the maximum and minimum value of the stress. The volumetric change rate of the CVD diamond ($\Delta V/V$) caused by the stress tensor can be delivered from the sum of the trace of the stress tensor ($\sigma_{xx} + \sigma_{yy} + \sigma_{zz}$), as shown in the following equation:

$$\frac{\Delta V}{V} = \frac{V - V'}{V} = -(\sigma_{xx} + \sigma_{yy} + \sigma_{zz}) (s_{11} + 2s_{12}), \quad (10)$$



27 November 2025 07:04:33

FIG. 3. (a-1)–(a-4) Spatial map of the stress tensor components (σ_{xy} , σ_{yz} , σ_{zx} , $\sigma_{xx} + \sigma_{yy} + \sigma_{zz}$) of stress tensor components around the threading defect, respectively. (b-1)–(b-4) Spatial map of measurement error of stress tensor components (σ_{xy_error} , σ_{yz_error} , σ_{zx_error} , $\sigma_{xx} + \sigma_{yy} + \sigma_{zz_error}$) around the threading defect, respectively. (c-1)–(c-4) ODMR spectra measured at the positions of A, B, C, and D shown in (b-4), respectively. (d) Experiment result of the diamond Raman peak shift around the threading defect. (e) Calculation result of the diamond Raman peak shift caused by the stress tensor around the threading defect.

where V is the initial volume and V' is the final volume through deformation due to stress applied, and $s_{11} = 0.952 \times 10^{-3}$ and $s_{12} = 0.099 \times 10^{-3} \text{ GPa}^{-1}$ are compliance constants⁴² (the derivation of this equation is described in the [supplementary material](#)). The tensile stress of $\sigma_{xx} + \sigma_{yy} + \sigma_{zz} = -1.2 \text{ GPa}$ was applied near the center of the threading defect. This means that the volume of the diamond crystal was increased approximately $6 \times 10^{-2}\%$ near the center of the threading defect.

Figures 3(b-1)–3(b-4) show the spatial map of the measurement error of the stress tensor, σ_{xy} , σ_{yz} , σ_{zx} and $\sigma_{xx} + \sigma_{yy} + \sigma_{zz}$, around the threading defect, respectively. The measurement error

of σ_{xy} , σ_{yz} , σ_{zx} and $\sigma_{xx} + \sigma_{yy} + \sigma_{zz}$ was approximately under 0.025, 0.025, 0.025, and 0.05 GPa, respectively, in most areas, although regions with measurement error exceeding 0.1 GPa were observed, as shown in Figs. 3(b-1)–3(b-4). The areas with high measurement errors of approximately 0.1 GPa correspond to regions where step bunching occurs on the CVD diamond film, as indicated by the optical microscope (OM) image and PL image shown in Figs. 2(a) and 2(f). Figures 3(c-1)–3(c-4) show the ODMR spectra at positions A, B, C, and D, as indicated in Fig. 3(b-4). Compared to position A, which had low measurement error, the baseline indicated by the red line in Fig. 3(c-1) was curved on the ODMR

spectra at points B, C, and D, leading to high fitting errors and high measurement error of stress. Decreasing the measurement error is essential for evaluating smaller stress variations below 0.1 GPa, such as the stress tensor of a single dislocation. Although we have not clarified the reason why the baseline of ODMR was curved induced by step bunching, we considered that the introduction of the Ramsey sequence⁴³ is effective for reducing measurement errors. In the Ramsey sequence, the difference (or ratio) between the off resonance and on-resonance intensities of the ODMR signal can be determined, leading to improved baseline accuracy (the measurement error of the stress tensor in this study was discussed in detail from the viewpoints of the stability of the conversion matrix from NV frequencies to the stress tensor and of error propagation in the [supplementary material](#)).

Next, to verify the reliability of the stress tensor obtained in this study, we compared the stress tensor measured by NV centers with stress measured by a conventional method, Raman spectroscopy. (The experimental method was described in detail in our previous study.²⁵) The change in the wavenumber of the diamond Raman peak indicated that stress was caused near the center of the threading defect. [Figure 3\(d-1\)](#) shows the Raman peak shift image near the threading defect. Subsequently, we calculated the Raman shift mapping from the stress tensor obtained using the NV centers. Typically, a given stress tensor modifies the phonon modes of diamond, changing the two transverse optical (TO) phonon modes and one longitudinal optical (LO) phonon mode to shift. As a result, the Raman peak of diamond—the frequency of the triply degenerate phonon—splits into three peaks. Please note that, in our experimental setup, only the LO phonon mode was detected based on the Raman selection rule (details are provided in the [supplementary material](#)). Assuming hydrostatic pressure ($\sigma_{xx} = \sigma_{yy} = \sigma_{zz} = (\sigma_{xx} + \sigma_{yy} + \sigma_{zz})/3$) and using the component of shear stress (σ_{xy} , σ_{yz} , σ_{zx}) measured by the NV centers, we calculated the Raman shift of the LO phonon mode, and the result is shown [Fig. 3\(e\)](#) (the detailed calculation procedure is provided in the [supplementary material](#)). Near the step-bunching region, where the measurement error of the stress tensor exceeded 0.1 GPa, a difference of approximately 0.4 cm^{-1} was observed between the experimental and calculated Raman shifts. In contrast, around the threading defect, the area in which the Raman shift was calculated

to change was comparable to the measurement results shown in [Fig. 3\(d-1\)](#). Furthermore, comparing the maximum and minimum Raman shift values, the Raman shift was calculated to be decreased about 0.9 cm^{-1} at the center of the threading dislocation, which was comparable to the experimental results. Therefore, we considered that the components of the stress tensor measured by NV centers accurately reflect the stress induced by the threading defects. In other words, in this study, we were able to extract components of the stress tensor that could not be distinguished by conventional measurement techniques.

Structure analysis

This threading defect was analyzed in detail by combining the stress tensor obtained in this study with data obtained from x-ray topography, in order to clarify its structure. [Figures 4\(a\)–4\(c\)](#) show the x-ray topography images near the threading defect. The diffraction vector \mathbf{g} of x-ray topography images in [Figs. 4\(a\)–4\(c\)](#) was $\mathbf{g} = [\bar{2}24]$, $[044]$, and $[404]$, respectively. When the Burgers vector of a dislocation is denoted as \mathbf{b} , the dislocation image disappears when $\mathbf{b} \cdot \mathbf{g} = 0$, whereas it becomes visible when $\mathbf{b} \cdot \mathbf{g} \neq 0$. The black lines in [Figs. 4\(b\)](#) and [4\(c\)](#) disappeared when \mathbf{g} was $[\bar{2}24]$. This result confirmed that these lines were dislocations with Burgers vector of $\mathbf{b} = [\bar{1}10]$, as shown in [Fig. 4\(d\)](#). Kato *et al.* have also reported that edge dislocations with $\mathbf{b} = [\bar{1}10]$ dominantly exist in (001) CVD diamond films,¹⁹ making this result consistent with our result. On the other hand, the diameter of the darker area of the threading defect measured in this study, indicated by the red circle, was larger than that of dislocation with a single Burgers vector. In addition, the image of the threading defect does not disappear under any \mathbf{g} vectors. These results means that this threading defect was not a single dislocation. We compared the stress field of this threading defect to that of single edge dislocation. In elasticity theory,⁴⁴ the trace of the stress tensor ($\sigma_{xx} + \sigma_{yy} + \sigma_{zz}$) generated by single edge dislocations is applied in the range diameter of approximately $4 \mu\text{m}$ from the center of the dislocation in diamonds (the image of the stress tensor around single edge dislocation estimated by elastic theory is shown in the [supplementary material](#)). As shown in [Fig. 3\(a\)](#), the area affected by the trace of the stress tensor ($\sigma_{xx} + \sigma_{yy} + \sigma_{zz}$) was approximately $10\text{--}15 \mu\text{m}$ diameter from the

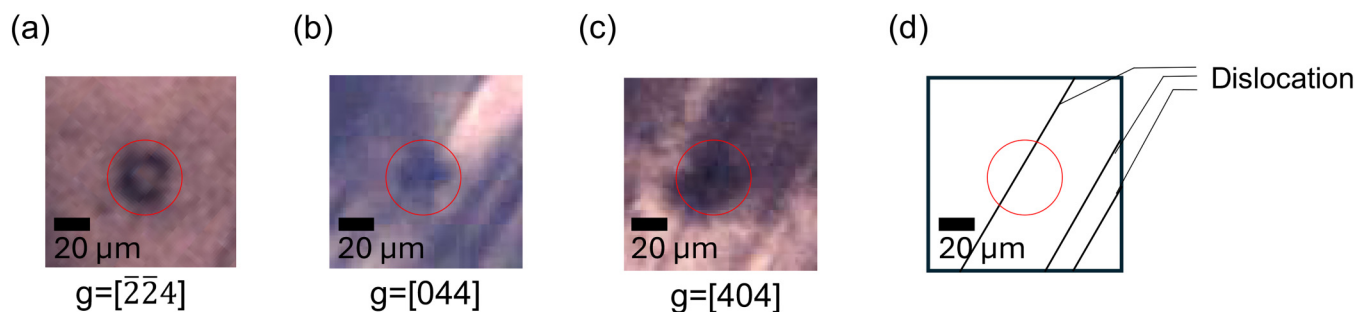


FIG. 4. (a)–(c) X-ray topography images near the threading defect. The diffraction vector \mathbf{g} of each image was $\mathbf{g} = [\bar{2}24]$, $[044]$, and $[404]$, respectively. (d) The schematic of the positions of threading defects and dislocations.

27 November 2025 07:04:33

center of the threading defect. Thus, the area affected by the stress of the threading defects was approximately three to four times larger than that by single dislocation. Furthermore, Ichikawa *et al.* have reported that the Raman peak position shifted by approximately 0.1 cm^{-1} near the center of a single dislocation.⁴⁵ As presented in Fig. 3(d), comparing the maximum and minimum Raman shift values, the Raman peak position near the center of the threading defect decreased by approximately -0.9 cm^{-1} . These results mean that the threading defect measured in this study had greater stress than a single dislocation. These results suggest that this threading defect was bundle dislocation.

CONCLUSION

We demonstrated the spatial imaging of the stress tensor around the threading defect propagated from the HPHT substrate in the nitrogen-doped CVD diamond film. We found that the distribution of the shear stress components, σ_{xy} , σ_{yz} , σ_{zx} , exhibited a point-symmetric stress distribution with respect to the center of the threading defect. In addition, the dominant component of the stress tensor induced by the threading defect was tensile stress with a magnitude of approximately 1.2 GPa. This tensile stress increased the volume of the diamond crystal near the center of the threading defect by approximately $6 \times 10^{-2}\%$. The magnitude and the spatial distribution of stress tensor components measured by the NV center were consistent with the Raman peak shift image. The stress tensor obtained in this study and x-ray topography images suggest that this threading defect was a bundle dislocation.

SUPPLEMENTARY MATERIAL

See the [supplementary material](#) for the details of the experiment method, measurement errors, calculation method of Raman peak shift caused by stress tensor, stress tensor of a single edge and screw dislocation, and benchmark of experiment specification in this study comparing that in the previous studies.

ACKNOWLEDGMENTS

This work was partially supported by MEXT Q-LEAP (No. JPMXS0118068379), JST Moonshot R&D (No. JPMJMS2062), CSTI SIP “Promoting the application of advanced quantum technology platforms to social issues,” JST ASPIRE (No. JPMJAP24C1), and JSPS KAKENHI (Nos. 24H00406 and 24K22963). We acknowledge Ms. Mai Nakashima from the Japan Advanced Institute of Science and Technology for fruitful discussion.

AUTHOR DECLARATIONS

Conflict of Interest

The authors have no conflicts to disclose.

Author Contributions

Takeyuki Tsuji: Conceptualization (lead); Data curation (lead); Formal analysis (lead); Funding acquisition (equal); Investigation (lead); Methodology (lead); Project administration (lead); Resources (lead); Software (lead); Validation (lead); Visualization (lead); Writing – original draft (lead). **Shunta Harada:** Funding

acquisition (equal); Resources (equal); Supervision (equal); Writing – review & editing (equal). **Tokuyuki Teraji:** Funding acquisition (equal); Project administration (equal); Resources (lead); Writing – review & editing (equal).

DATA AVAILABILITY

The data that support the findings of this study are available from the corresponding author upon reasonable request.

REFERENCES

- C. J. H. Wort and R. S. Balmer, “Diamond as an electronic material,” *Mater. Today* **11**(1–2), 22–28 (2008).
- H. Kawarada, M. Aoki, and M. Ito, “Enhancement mode metal-semiconductor field effect transistors using homoepitaxial diamonds,” *Appl. Phys. Lett.* **65**(12), 1563–1565 (1994).
- C. E. Nebel, “CVD diamond: A review on options and reality,” *Funct. Diamond* **3**(1), 1–10 (2023).
- J. F. Barry, J. M. Schloss, E. Bauch, M. J. Turner, C. A. Hart, L. M. Pham, and R. L. Walsworth, “Sensitivity optimization for NV-diamond magnetometry,” *Rev. Mod. Phys.* **92**(1), 015004 (2020).
- S. Praver and A. D. Greentree, “Applied physics. Diamond for quantum computing,” *Science* **320**(5883), 1601–1602 (2008).
- H. Kurokawa, M. Yamamoto, Y. Sekiguchi, and H. Kosaka, “Remote entanglement of superconducting qubits via solid-state spin quantum memories,” *Phys. Rev. Appl.* **18**(6), 064039 (2022).
- N. Aslam, H. Zhou, E. K. Urbach, M. J. Turner, R. L. Walsworth, M. D. Lukin, and H. Park, “Quantum sensors for biomedical applications,” *Nat. Rev. Phys.* **5**(3), 157–169 (2023).
- J. R. Maze, P. L. Stanwix, J. S. Hodges, S. Hong, J. M. Taylor, P. Cappellaro, L. Jiang, M. V. G. Dutt, E. Togan, A. S. Zibrov, A. Yacoby, R. L. Walsworth, and M. D. Lukin, “Nanoscale magnetic sensing with an individual electronic spin in diamond,” *Nature* **455**(7213), 644–647 (2008).
- L. Childress and R. Hanson, “Diamond NV centers for quantum computing and quantum networks,” *MRS Bull.* **38**(2), 134–138 (2013).
- K. Nemoto, M. Trupke, S. J. Devitt, B. Scharfenberger, K. Buczak, J. Schmiedmayer, and W. J. Munro, “Photonic quantum networks formed from NV[−] centers,” *Sci. Rep.* **6**(1), 26284 (2016).
- S.-H. Wei, B. Jing, X.-Y. Zhang, J.-Y. Liao, C.-Z. Yuan, B.-Y. Fan, C. Lyu, D.-L. Zhou, Y. Wang, G.-W. Deng, H.-Z. Song, D. Oblak, G.-C. Guo, and Q. Zhou, “Towards real-world quantum networks: A review,” *Laser Photonics Rev.* **16**(3), 2100219 (2022).
- Y. Sekiguchi, K. Matsushita, Y. Kawasaki, and H. Kosaka, “Optically addressable universal holonomic quantum gates on diamond spins,” *Nat. Photonics* **16**(9), 662–666 (2022).
- F. Jelezko, T. Gaebel, I. Popa, M. Domhan, A. Gruber, and J. Wrachtrup, “Observation of coherent oscillation of a single nuclear spin and realization of a two-qubit conditional quantum gate,” *Phys. Rev. Lett.* **93**(13), 130501 (2004).
- D. Budker and M. Romalis, “Optical magnetometry,” *Nat. Phys.* **3**(4), 227–234 (2007).
- F. Dolde, H. Fedder, M. W. Doherty, T. Nöbauer, F. Rempp, G. Balasubramanian, T. Wolf, F. Reinhard, L. C. L. Hollenberg, F. Jelezko, and J. Wrachtrup, “Electric-field sensing using single diamond spins,” *Nat. Phys.* **7**(6), 459–463 (2011).
- B. Yang, T. Murooka, K. Mizuno, K. Kim, H. Kato, T. Makino, M. Ogura, S. Yamasaki, M. E. Schmidt, H. Mizuta, A. Yacoby, M. Hatano, and T. Iwasaki, “Vector electrometry in a wide-gap-semiconductor device using a spin-ensemble quantum sensor,” *Phys. Rev. Appl.* **14**(4), 044049 (2020).
- M. W. Doherty, V. M. Acosta, A. Jarmola, M. S. J. Barson, N. B. Manson, D. Budker, and L. C. L. Hollenberg, “Temperature shifts of the resonances of the NV[−] center in diamond,” *Phys. Rev. B* **90**(4), 041201 (2014).

- ¹⁸Y. Hatano, J. Shin, D. Nishitani, H. Iwatsuka, Y. Masuyama, H. Sugiyama, M. Ishii, S. Onoda, T. Ohshima, K. Arai, T. Iwasaki, and M. Hatano, "Simultaneous thermometry and magnetometry using a fiber-coupled quantum diamond sensor," *Appl. Phys. Lett.* **118**(3), 034001 (2021).
- ¹⁹Y. Kato, H. Umezawa, H. Yamaguchi, and S. Shikata, "X-ray topography used to observe dislocations in epitaxially grown diamond film," *Jpn. J. Appl. Phys.* **51**(9R), 090103 (2012).
- ²⁰A. Lohstroh, P. J. Sellin, S. G. Wang, A. W. Davies, J. Parkin, R. W. Martin, and P. R. Edwards, "Effect of dislocations on charge carrier mobility-lifetime product in synthetic single crystal diamond," *Appl. Phys. Lett.* **90**(10), 102111 (2007).
- ²¹A. Mussi, D. Eyidi, A. Shiryaev, and J. Rabier, "TEM observations of dislocations in plastically deformed diamond," *Phys. Status Solidi A* **210**(1), 191–194 (2013).
- ²²S. Ohmagari, H. Yamada, N. Tsubouchi, H. Umezawa, A. Chayahara, S. Tanaka, and Y. Mokuno, "Large reduction of threading dislocations in diamond by hot-filament chemical vapor deposition accompanying W incorporations," *Appl. Phys. Lett.* **113**(3), 032108 (2018).
- ²³T. Kimoto, "Material science and device physics in SiC technology for high-voltage power devices," *Jpn. J. Appl. Phys.* **54**(4), 040103 (2015).
- ²⁴S. Fujita, "Wide-bandgap semiconductor materials: For their full bloom†," *Jpn. J. Appl. Phys.* **54**(3), 030101 (2015).
- ²⁵T. Tsuji, C. Shinei, T. Iwasaki, M. Hatano, and T. Teraji, "Evaluation of stress in (111) homoepitaxial CVD diamond films by Raman spectrum and nitrogen-vacancy centers," *Appl. Phys. Express* **17**, 115502 (2024).
- ²⁶A. Barfuss, M. Kasperczyk, J. Kölbl, and P. Maletinsky, "Spin-stress and spin-strain coupling in diamond-based hybrid spin oscillator systems," *Phys. Rev. B* **99**(17), 174102 (2019).
- ²⁷Y. Narita, P. Wang, K. Ikeda, K. Oba, Y. Miyamoto, T. Taniguchi, S. Onoda, M. Hatano, and T. Iwasaki, "Multiple tin-vacancy centers in diamond with nearly identical photon frequency and linewidth," *Phys. Rev. Appl.* **19**(2), 024061 (2023).
- ²⁸S. Pezzagna and J. Meijer, "Quantum computer based on color centers in diamond," *Appl. Phys. Rev.* **8**(1), 011308 (2021).
- ²⁹T. Tsuji, T. Sekiguchi, T. Iwasaki, and M. Hatano, "Extending spin dephasing time of perfectly aligned nitrogen-vacancy centers by mitigating stress distribution on highly misoriented chemical-vapor-deposition Diamond," *Adv. Quantum Technol.* **7**, 2300194 (2024).
- ³⁰Y. von Kaenel, J. Stiegler, J. Michler, and E. Blank, "Stress distribution in heteroepitaxial chemical vapor deposited diamond films," *J. Appl. Phys.* **81**(4), 1726–1736 (1997).
- ³¹D. Howell, "Strain-induced birefringence in natural diamond: A review," *Eur. J. Mineral.* **24**(4), 575–585 (2012).
- ³²Y. Kato, H. Umezawa, and S.-I. Shikata, "X-ray topographic study of defect in p⁺ diamond layer of Schottky barrier diode," *Diamond Relat. Mater.* **57**, 22–27 (2015).
- ³³S. Hsieh, P. Bhattacharyya, C. Zu, T. Mittiga, T. J. Smart, F. Machado, B. Kobrin, T. O. Höhn, N. Z. Rui, M. Kamrani, S. Chatterjee, S. Choi, M. Zaletel, V. V. Struzhkin, J. E. Moore, V. I. Levitas, R. Jeanloz, and N. Y. Yao, "Imaging stress and magnetism at high pressures using a nanoscale quantum sensor," *Science* **366**(6471), 1349–1354 (2019).
- ³⁴D. A. Broadway, B. C. Johnson, M. S. J. Barson, S. E. Lillie, N. Donschuk, D. J. McCloskey, A. Tsai, T. Teraji, D. A. Simpson, A. Stacey, J. C. McCallum, J. E. Bradby, M. W. Doherty, L. C. L. Hollenberg, and J.-P. Tetienne, "Microscopic imaging of the stress tensor in diamond using *in situ* quantum sensors," *Nano Lett.* **19**(7), 4543–4550 (2019).
- ³⁵P. Kehayias, M. J. Turner, R. Trubko, J. M. Schloss, C. A. Hart, M. Wesson, D. R. Glenn, and R. L. Walsworth, "Imaging crystal stress in diamond using ensembles of nitrogen-vacancy centers," *Phys. Rev. B* **100**(17), 174103 (2019).
- ³⁶L. Rondin, J.-P. Tetienne, T. Hingant, J.-F. Roch, P. Maletinsky, and V. Jacques, "Magnetometry with nitrogen-vacancy defects in diamond," *Rep. Prog. Phys.* **77**(5), 056503 (2014).
- ³⁷T. Teraji and C. Shinei, "Nitrogen-related point defects in homoepitaxial diamond (001) freestanding single crystals," *J. Appl. Phys.* **133**(16), 165101 (2023).
- ³⁸T. Teraji, J. Isoya, K. Watanabe, S. Koizumi, and Y. Koide, "Homoepitaxial diamond chemical vapor deposition for ultra-light doping," *Mater. Sci. Semicond. Process.* **70**, 197–202 (2017).
- ³⁹T. Teraji, "High-quality and high-purity homoepitaxial diamond (100) film growth under high oxygen concentration condition," *J. Appl. Phys.* **118**(11), 115304 (2015).
- ⁴⁰M. N. R. Ashfold, J. P. Goss, B. L. Green, P. W. May, M. E. Newton, and C. V. Peaker, "Nitrogen in diamond," *Chem. Rev.* **120**(12), 5745–5794 (2020).
- ⁴¹S. Harada and K. Murayama, "Observation of in-plane shear stress fields in off-axis SiC wafers by birefringence imaging," *J. Appl. Crystallogr.* **55**(4), 1029–1032 (2022).
- ⁴²M. Mermoux, B. Marcus, A. Crisci, A. Tajani, E. Gheeraert, and E. Bustarret, "Micro-Raman scattering from undoped and phosphorous-doped (111) homoepitaxial diamond films: Stress imaging of cracks," *J. Appl. Phys.* **97**(4), 043530 (2005).
- ⁴³E. Bauch, S. Singh, J. Lee, C. A. Hart, J. M. Schloss, M. J. Turner, J. F. Barry, L. M. Pham, N. Bar-Gill, S. F. Yelin, and R. L. Walsworth, "Decoherence of ensembles of nitrogen-vacancy centers in diamond," *Phys. Rev. B* **102**(13), 134210 (2020).
- ⁴⁴D. Hull and D. J. Bacon, *Introduction to Dislocation* (Oxford, England, 2011).
- ⁴⁵K. Ichikawa, T. Shimaoka, Y. Kato, S. Koizumi, and T. Teraji, "Dislocations in chemical vapor deposition diamond layer detected by confocal Raman imaging," *J. Appl. Phys.* **128**(15), 155302 (2020).